

Implications of phonon anisotropy on thermal conductivity of fluorite oxides

Saqeeb Adnan¹, Miaomiao Jin², Matthew S Bryan³, Michael E Manley³ and David H. Hurley⁴, Marat Khafizov^{1‡}

¹ Department of Mechanical and Aerospace Engineering, The Ohio State University, Columbus, OH 43210, USA

² Department of Nuclear Engineering, The Pennsylvania State University, University Park, PA 16802, USA

³ Oak Ridge National Laboratory, Oak Ridge, TN 37830, USA

⁴ Idaho National Laboratory, Idaho Falls, ID 84315, USA

Fluorite oxides are attractive ionic compounds for a range of applications with critical thermal management requirements. In view of recent reports alluding to anisotropic thermal conductivity in face-centered cubic crystalline systems, we perform a detailed analysis of the impact of direction-dependent phonon group velocities and lifetimes on thermal transport (i.e. phonon anisotropy). In this article, we aim to investigate the implication of the anisotropic features on the mode resolved contribution to thermal conductivity. We observe that for accurate determination of thermal conductivity it is not adequate to only consider phonon properties along high symmetry directions. While the bulk thermal conductivity of this class of materials is isotropic, we show that breaking the symmetry of the phonon lifetime under external stimuli such as boundary scattering gives rise to anisotropic thermal conductivity.

I. INTRODUCTION

First-principles understanding phonon-mediated thermal transport in fluorite oxides with lanthanide and actinide elements as cation has been complicated by competing effects of lattice anharmonicity and electron correlation effects [1–3]. Analysis of harmonic and anharmonic properties depends on precise computation of interatomic forces which is related to the ability to accurately describe the electronic structure of the system [4]. While different methods to improve the electronic structure calculations in strongly electron correlated systems are available, the implications of these methods to the accuracy of thermal transport prediction are not known. Uranium dioxide (UO₂) is an example system where understanding thermal transport from first principles has been challenging [1,3]. In order to determine the adequacy of a simplified description of the correlation effects for a reliable prediction of phonon properties, it is important to understand phonon dispersion and lifetime. Examples include the contribution of optical phonons to thermal transport, the emergence of resolvable Raman active vibration modes when defects are present, and anharmonicity [1,5–9]. Here, we focus on phonon properties that depend on propagation direction in thorium dioxide (ThO₂) as a model fluorite system [5,10]. This

detailed characterization of phonon anisotropy in ThO₂ provides a baseline for other fluorites and assists in future studies focusing on the isolation of electron correlation effects on phonon structure and thermal transport.

While acoustic anisotropy characterized by directional dependence of the bulk plane wave propagation in solids with cubic symmetries is well known [10,11], several recent reports have entertained a concept of thermal conductivity anisotropy in cubic fluorites [12–14]. The detailed analysis, presented here, of the phonon anisotropy in ThO₂ will shed light on this controversial topic. We define phonon anisotropy in the same spirit as acoustic anisotropy. Figure 1 depicts surface plots of phonon phase velocity for selected phonon branches in ThO₂ obtained from the solution of the dynamical matrix [5,15]. It represents the magnitude of the velocity of phonons propagating along different directions lying on the q-space iso-surface. The surface plots for acoustic phonons closely resemble the shape of the bulk acoustic velocities obtained from the solution of the Christoffel equation [11]. Acoustic modes exhibit a modest departure from the surface of the sphere, where LA (longitudinal acoustic) mode is close to directionally independent, while the TA (transverse acoustic) modes exhibit noticeable anisotropy. The velocity surface plot of the optical modes,

‡ khafizov.1@osu.edu

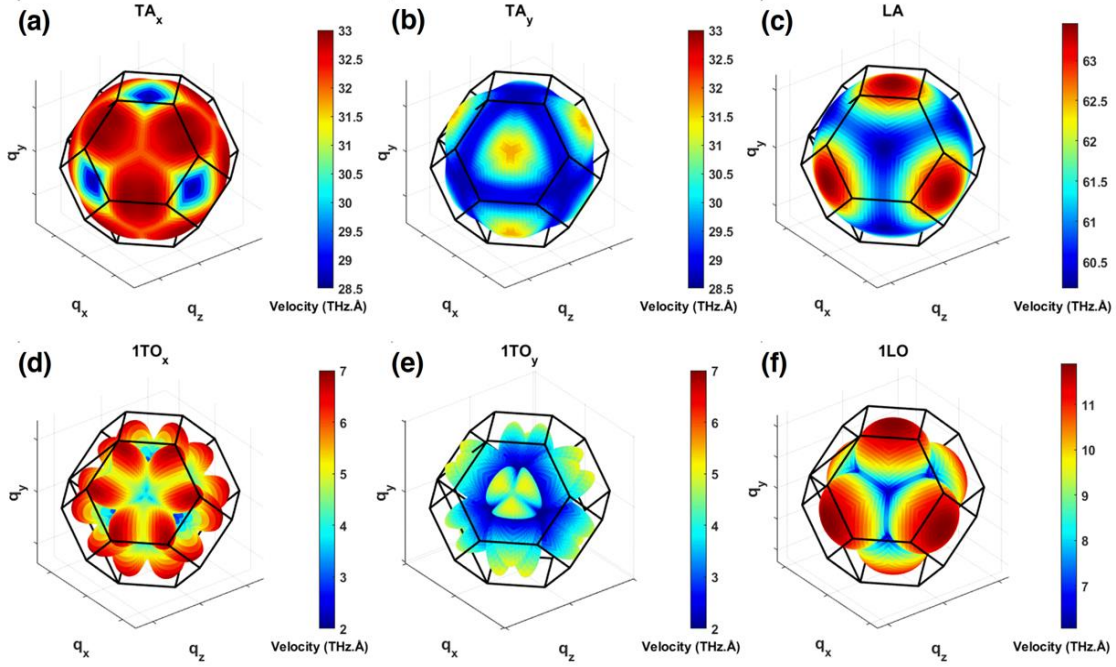


FIG. 1. 3D phonon velocity plots for $q = 0.1 \frac{2\pi}{a}$ for acoustic (a) TA_x (b) TA_y (c) LA modes and optic (d) $1TO_x$ (e) $1TO_y$ (f) $1LO$ modes based on IFCs reported in [5].

on the other hand, exhibit complex structures having strong directional dependence and is thus classified as highly anisotropic.

Our classical understanding of lattice dynamics relies on measurements of phonons using inelastic neutron scattering experiments [1,16]. Early measurements employed nuclear reactor-derived neutrons utilizing triple-axis inelastic neutron scattering. This significantly limited the number of measurements and therefore has mostly been limited to measurement along high symmetry directions [16]. Novel instruments which utilize higher neutron fluxes derived from spallation sources such as wide-angle range time-of-flight neutron measurements allow measuring phonon dispersion over a broader range of phonon wavelength in a single acquisition [17]. While instruments utilizing wide angular range chopper spectrometer (ARCS) have been shown to be very effective in measuring phonon dispersion curves [18], isolating phonon lifetime from linewidths measurements is still complicated by an instrument resolution and requires further advancements before direct comparison to first-principles calculations is viable [19].

Thorium dioxide (ThO_2) is used as a model for fluorite oxides including uranium dioxide (UO_2), cerium dioxide (CeO_2), and YSZ (Yttria-stabilized zirconia). UO_2 is the most extensively used commercial nuclear fuel [2], CeO_2 and YSZ have applications in the electrochemical energy sector i.e., solid oxide fuel cell (SOFC) [20–22],

while YSZ is also used as a thermal barrier coating. ThO_2 is also a surrogate for modeling UO_2 and CeO_2 properties using first-principles methods, as it offers an identical crystal structure, but complications associated with the treatment of f -electrons correlation effects are avoided [23,24]. Its large optical bandgap makes it attractive as a laser host material. Most of these applications demand a detailed understanding of its thermal transport.

Phonons and thermal conductivity in ThO_2 and related compounds have seen renewed interest lately. Phonon dispersion primarily determined by harmonic interactions has been investigated both experimentally [16] and theoretically [25,26]. At and above room temperature, lattice thermal conductivity is mainly limited by the phonon-phonon scattering, an intrinsic phenomenon arising from crystal anharmonicity [27]. Measurement and modeling of anharmonic properties including phonon lifetimes have started to receive some attention [19]. Theoretical calculations of lattice thermal conductivity of ThO_2 using non-equilibrium molecular dynamics (NEMD) employing empirical interatomic potentials (EIP) [13,28,29], Slack method [30], and solution of Boltzmann transport equation (BTE) by using interatomic forces from ab-initio density functional theory (DFT) [5,25,31] have been reported. The impact of point defects, impurities, and grain boundaries resulting in additional phonon scattering in reducing thermal conductivity [32] have also been investigated [7,33,34]. A

thorough discussion of these studies and several others can be found in a recent review article [2].

In this work, we investigate the impact of phonon anisotropy on lattice thermal conductivity within first-principles-based BTE formalism. We compare two different approaches to compute lattice thermal conductivity. The first considers all the phonons, and the second represents the phonons using only high symmetry directions. Such an approach helps us demonstrate the importance of considering phonons along low-symmetry directions. By analyzing the spectral conductivity profiles, we found a significant contribution from the off-axial phonons to thermal conductivity. In order to correlate these features with phonon properties, we carefully examine the phonon lifetimes and velocities in all the directions in the q-space. While our results demonstrate strong evidence of phonon anisotropy, the bulk thermal conductivity in ThO₂ or other fluorites remains isotropic due to O_h cubic symmetry [35]. Next, we demonstrate how phonon anisotropy manifests itself in NEMD-based calculations in small simulation cells exhibiting size effect. These cell size-dependent results are found to be consistent with a simple BTE analysis including boundary scattering that captures the size effects and lifts the symmetry of the phonon lifetimes. Finally, we investigate the implications of the phonon anisotropy on phonon-defect scattering using a formulation developed for treating isotopic scattering of phonons. Together these analyses provide a comprehensive insight into the implication of phonon anisotropy in ThO₂.

II. METHODS

To calculate the thermal conductivity of ThO₂, we used Boltzmann Transport Equation (BTE) formalism under the relaxation time approximation as implemented within the Phono3py code [36,37]. The conductivity tensor $k_{\alpha\beta}$ is computed using

$$k_{\alpha\beta} = \frac{1}{V_0} \sum_{\mathbf{q}, m} C_{\mathbf{q}, m} v_{\mathbf{q}, m, \alpha} v_{\mathbf{q}, m, \beta} \tau_{\mathbf{q}, m} \quad (1)$$

Here, $v_{\mathbf{q}, m}$, $C_{\mathbf{q}, m}$ and $\tau_{\mathbf{q}, m}$ are the group velocity, mode heat capacity, and phonon relaxation time of the phonon mode, m , defined by the phonon wavenumber (\mathbf{q}) in reciprocal space. V_0 is the volume of a unit cell. Conductivity ($k_{\hat{n}}$) along a particular direction \hat{n} can be calculated after replacing $v_{\alpha} v_{\beta}$ in Eq. 1 by $|v_{\mathbf{q}, m} \cdot \hat{n}|^2$. In this formulation, k includes the contribution from phonons propagating in all directions in the q-space. To emphasize the impact of phonon anisotropy, we employ an alternative definition of conductivity that considers only phonons

along high symmetry directions $[00\xi]$, $[\xi 0\xi]$, $[\xi\xi\xi]$, which are traditionally measured using inelastic neutron scattering employing triple-axis spectrometer [16]. In this method, the whole Brillouin zone is approximated using the high-symmetry (axial) sampling points [1] and conductivity of single branch contribution is given by:

$$k_m^{(HS)} = \sum_{i=1}^{N_d} \Omega_i \int_0^{q_{\max, i}} C_{q, m} \frac{v_{q, m}^2}{3} \tau_{q, m} q^2 dq \quad (2)$$

Here, conductivity is calculated by the sum over selected directions in q-space. When considering high symmetry phonons, the solid angle constitutes three classes of phonons. Solid angle (Ω) for each equivalent direction (6 along $[00\xi]$, 12 – $[\xi 0\xi]$, and 8 – $[\xi\xi\xi]$) denoted by subscript i , are determined to be $\Omega_{[00\xi]} = 0.50$, $\Omega_{[\xi 0\xi]} = 0.58$, and $\Omega_{[\xi\xi\xi]} = 0.33$ and $N_d = 26$ [1]. The results using this formulation are termed as ‘high-symmetry’ calculation from here on. In the case of isotropic phonons only one direction with a solid angle of $\Omega = 4\pi$ is considered and Eq.2 is reduced to a classical analytical expression [38].

To compute the parameters needed for thermal conductivity calculation including interatomic force constants (IFCs), we used phonopy [39] and phono3py [37] software packages. The second (2IFC) and third (3IFC) order IFCs were determined using CRG potential and DFT based on the finite displacement method with a displacement step of 0.03 Å following Jin *et. al* [5]. The LAMMPS [40] package was used to calculate the forces of displaced supercell structure using an empirical interatomic force field based on CRG potential [41]. DFT calculations were implemented within VASP [42] where the electronic exchange-correlation was described using local density approximation (LDA) [43]. 2IFCs were used to construct a dynamical matrix for the calculation of phonon dispersions and 3IFCs were used to compute 3-phonon scattering rates. Results obtained from the DFT approach using the LDA will be denoted as DFT-LDA whereas results obtained using CRG potential will be denoted with EIP-CRG. The conventional unit cell consisting of 12 atoms is fully relaxed and their lattice constants are 5.529 Å and 5.580 Å for DFT-LDA and EIP-CRG, respectively. To calculate the 2IFCs, 3×3×3 supercells are generated consisting of 324 atoms, while 2×2×2 supercells of 96 atoms are used for 3IFCs. Further computational have been previously reported in [5]. Elastic constants calculated using these two approaches are $C_{11} = 352$, $C_{12} = 113$ and $C_{44} = 72$ GPa and $C_{11} = 380$, $C_{12} = 130$ and $C_{44} = 96$ GPa, for EIP-CRG and DFT-LDA, respectively. These values compare favorably with

experimental data, reporting $C_{11} = 361$, $C_{12} = 115$, and $C_{44} = 78$ GPa [44]. These values result in acoustic anisotropy represented by Zener ratios (r) of 0.602 and 0.768 for CRG and LDA, respectively. This indicates large anisotropy of phonon derived from EIP-CRG, which agrees better with the experimental value of 0.63.

The mode assignment of 9 phonon modes resulting from a 3 atom unit cell as TA_x , TA_y , LA , $1TO_x$, $1TO_y$, $1LO$, $2TO_x$, $2TO_y$, and $2LO$ was performed based on the eigenvector analysis [45]. A and O refer to acoustic and optic modes, respectively. T and L correspond to modes having a primarily longitudinal and transverse displacement of atoms with respect to the direction of \mathbf{q} . Subscripts x and y distinguish two transverse modes, by their primary polarization along the x and y-axis when \mathbf{q} is defined with irreducible BZ confined by [001], [101], [111] directions. Eigenvectors of these modes contain information regarding the relative movements of the atoms i.e., the acoustic modes are primarily related to the vibration of heavier thorium ions whereas the optical modes are governed by the motion of oxygen ions. The mode assignment is done by first taking eigenvectors of the nine degenerate modes along $[\xi 0 \xi]$ direction as a reference for each mode label. Then the projection of different phonons along those reference modes is calculated by using the dot product of the phonon's mode eigenvector and each reference. The mode with the largest projection is assigned to that mode.

Inelastic neutron scattering (INS) measurements were performed to experimentally measure the dispersion of ThO_2 . Time-of-flight inelastic neutron scattering measurements were performed on a single crystal of ThO_2 at 300 K, as described elsewhere [17] using the wide Angular Range Chopper Spectrometer (ARCS) [18]. A pulse of monochromatic incoming neutrons exchanges energy and momentum with the sample. Position sensitive detectors measure the scattered neutron intensity as a function of angle and time, which is then converted into scattered intensity as a function of momentum and energy transfer. Multiple Brillouin zones are contained in the full data set and scattering as a function of energy is analyzed along the high symmetry directions.

The phonon dispersion and linewidths measured with INS can in principle be used to determine $v_{\mathbf{q},m}$ and $\tau_{\mathbf{q},m}$, respectively. The results obtained from ARCS can be readily processed to construct phonon dispersions and direct comparison to model results. However, for phonon linewidths, which are inversely proportional to phonon lifetime, the comparison is not straightforward, and one needs to account for instrumental broadening. The INS measurements of ThO_2 contain the relaxation time of a small volume in reciprocal space, in contrast to the points

in reciprocal space that are produced by simulation. The volume size is adjustable during data analysis but limited by instrumentation, and sample size among other factors. There is an appreciable change in relaxation time across the volume measured by INS, and as a result, the INS relaxation times are an average over the measured volume. This is in contrast to simulation results which occur at a single point in reciprocal space, and a direct comparison does not yield an agreement. Simulating a volume identical to the measured INS volume is required. The phonon dispersion does not appear to be sensitive to this effect. A detailed discussion of this subject is beyond the scope of this manuscript [19].

Non-equilibrium molecular dynamics (NEMD) as implemented in the LAMMPS [40] package is also used to calculate the thermal conductivity along different crystal orientations. The interatomic interactions are described by the CRG potential [41]. An elongated simulation cell having periodic boundary conditions along all directions is constructed as two regions are set to be hot and cold zones, respectively. The temperature of the two regions is controlled via the Langevin thermostat. The thermal conductivity is calculated using Fourier's law after a stable linear temperature profile and constant heat flux are established. For this study, data are collected over 1 ns long simulation employing the microcanonical ensemble with a time step of 0.001 ps. The length of the simulation cell is varied to capture the size effect on thermal conductivity. For each simulation cell length, three sets of calculations are performed with different initializing random seeds in order to improve statistical accuracy.

III. PHONON ANISOTROPY

A. Phonon dispersion

We start by analyzing the phonon dispersion curves for ThO_2 . In Fig. 2, we present the experimental results obtained from inelastic neutron scattering compared to the DFT-LDA results. Experimental dispersion for high symmetry directions along Γ -X $[\xi 0 0]$, Γ -K $[\xi \xi 0]$, and Γ -L $[\xi \xi \xi]$ have been previously reported [17], whereas X-W direction is reported for the first time. Model dispersion curves include additional low symmetry direction such as Γ -W $[2\xi, \xi, 0]$ and X-L. It should be noted here that in fact Γ -W direction has higher symmetry than Γ -K, but in this manuscript, we still treat Γ -W as a part of low symmetry, to keep with the historic trend where Γ -K has been more frequently reported.

The slopes of Γ -X, Γ -K, Γ -L, and Γ -W define the group velocity, from which initial assessment on the relative contribution of each phonon mode to thermal

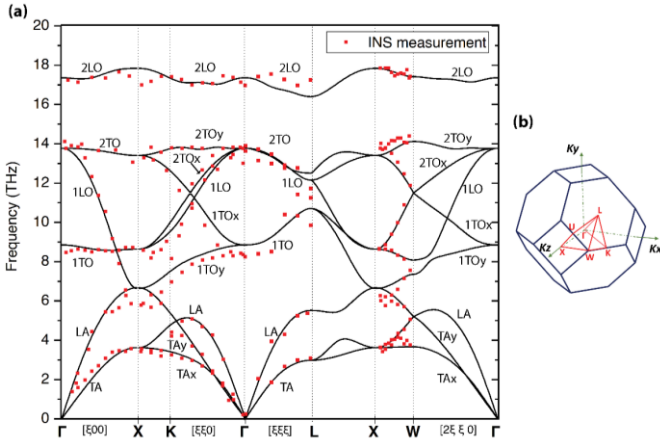


FIG. 2. (a) Phonon dispersion curves for ThO_2 using DFT-LDA and experimental results from INS. (b) First Brillouin zone and the irreducible Brillouin zone wedge (red).

conductivity can be performed. ThO_2 dispersion is represented by nine modes (three acoustic and six optical modes) corresponding to 9 degrees of freedom of the three atoms in the primitive cell [46]. The acoustic modes are classified into two transverse acoustic (TA) and longitudinal acoustic (LA) modes. Along Γ -X and Γ -K directions, the two transverse modes are degenerate, but this degeneracy is lifted along other directions. We distinguish TA modes based on the direction of atomic vibration and term them as TA_x and TA_y (polarized along the X and Y axis respectively for modes inside the irreducible BZ shown in Fig. 2b). Careful examination of dispersion curves reveals a strong anisotropy in TA_y mode. While LA mode branches along high symmetry directions overlap, i.e., they all have maxima at about 5 THz, the TA_y mode's branches are spread out where maximum frequency varies over 3- 6 THz range along different directions. Acoustic modes have large slopes as generally expected and should contribute significantly to the conductivity of ThO_2 [1,47-49]. Fluorite structures possess highly dispersive optical modes. It can be seen that the LO mode has a high group velocity along the Γ -X and Γ -K directions and its contribution to thermal transport has been discussed in several recent reports [1,3,6]. However, velocity along Γ -L direction is smaller. This highly anisotropic nature of optical modes is best captured in Fig. 1(f). It should also be noted that 1TO_y while relatively flat along high symmetry directions, exhibits a large slope along the low-symmetry directions (Fig. 1 d and e).

Closer examination of dispersion along the X-W segment serves as experimental evidence of strong anisotropy in phonon structure. It approximates an arc on the sphere defined by constant k-magnitude. For isotropic

material, the frequency of individual modes should remain constant. A large variation of phonon frequencies along this path validated by INS measurements is a strong indication of phonon anisotropy in this fluorite system. Other cubic materials like diamond also have dispersion profiles with similar anisotropy in high symmetry direction whereas in silicon carbide the anisotropy is less obvious [50,51]. Dispersion curves based on IFC derived from EIP-CRG have comparable acoustic mode features, but optical modes are notably different [5]. Therefore, we treat EIP-CRG as a model that exhibits a different degree of anisotropy for the fluorite structure having an alternative dispersion curve.

B. Branch resolved high symmetry conductivity

The mode-specific thermal conductivity contributions calculated using DFT-LDA and EIP-CRG derived IFCs are depicted in a bar plot in Fig. 3. The results presented in red consider phonons along all directions, while results in blue consider only high symmetry modes. This helps compactly reveal anisotropic features and is also in keeping with historic measurements [16,17]. The total thermal conductivity found using the high symmetry method is 14.20 W/m·K, compared to 17.96 W/m·K using the all-phonon method in the case of LDA calculation. A similar calculation using EIP-CRG result in 16.64 vs 23.61 W/m·K

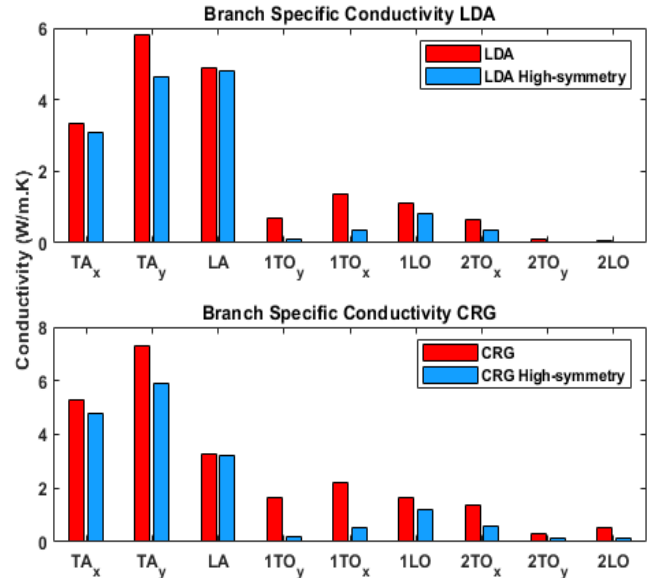


FIG. 3. Mode-specific thermal conductivity contribution for DFT-LDA and EIP-CRG using all-phonon (red bars and Eq.1) and high-symmetry phonon (blue bars and Eq.2) methods.

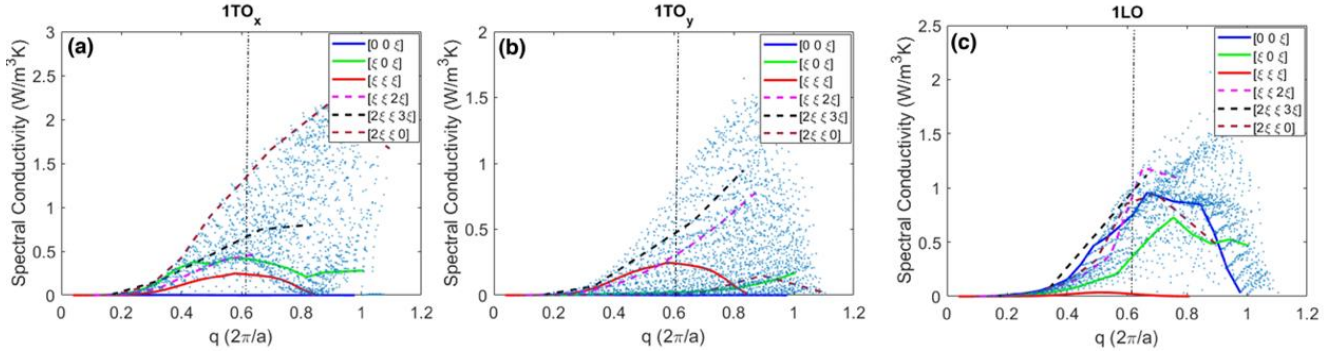


FIG. 4. Spectral conductivity profiles for optical modes (a) $1TO_x$ (b) $1TO_y$ and (c) $1LO$ using DFT-LDA. Spectral conductivity values are calculated by multiplying the thermal conductivity values with a weighting factor based on the q -point and phonon orientation.

– a much larger difference. The high symmetry method notably underestimates thermal conductivity. When one considers mode-specific conductivity, one observes higher values from the first method compared to the high-symmetry approach for most of the modes. While both approaches provide a comparable contribution from LA modes, the discrepancy is the largest for TA_y and all TO modes, which suggests that the low-symmetry direction might provide a greater contribution than the high symmetry phonons. Relative contributions trends for different modes are in agreement with the trends in phonon’s group velocity revealed from an analysis of dispersion curves discussed in Sec. III.A and in Fig. 2 and have been addressed in previous reports [1,5].

C. Spectral conductivity

The origin of the above-mentioned difference in thermal conductivity calculation can be inferred from careful analysis of a direction-dependent spectral conductivity for the optical and acoustic modes shown in Figs. 4-6. The spectral conductivity calculation for a

particular direction follows the procedure of high-symmetry calculations, but in this case, only the phonons along a particular direction are used to calculate total conductivity, essentially limiting the summation in Eq. 2 to one direction with a 4π solid angle, resulting in:

$$\frac{dk}{dq} = 4\pi C_{q,m} \frac{v_{q,m}^2}{3} \tau_{q,m} q^2 \quad (3)$$

Figure 4 shows the spectral conductivity profiles for three of the optical modes, namely $1LO$ and two $1TO$ modes. There is a noticeable directional dependence for $1LO$ mode, where $[\xi\xi\xi]$ direction has a very little contribution, whereas $[00\xi]$ direction has a very large contribution (Fig.4c). Similar anisotropic features are found in the $1TO_x$ mode (Fig.4a), however, one feature stands out for $1TO_x$ mode. While low symmetry directions in $1LO$ are mostly bounded by the high symmetry ones, the $[2\xi \xi 0]$ direction of $1TO_x$ mode is outside of the bounds defined by the high symmetry axis. Note that the other low symmetry direction phonons are represented by the scatter points. Considering this together with results in Fig. 3, strongly suggests that low symmetry directions contribute

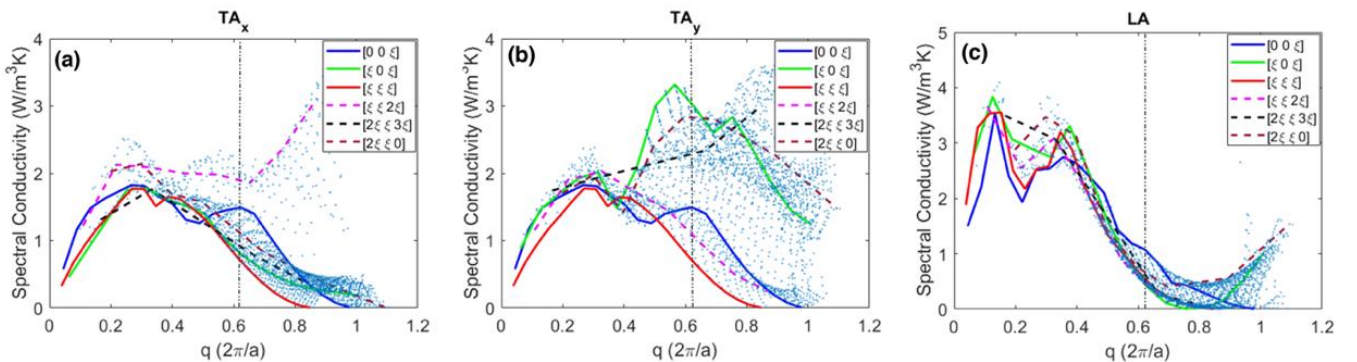


FIG. 5. Spectral conductivity profiles for acoustic modes (a) TA_x (b) TA_y and (c) LA using DFT-LDA.

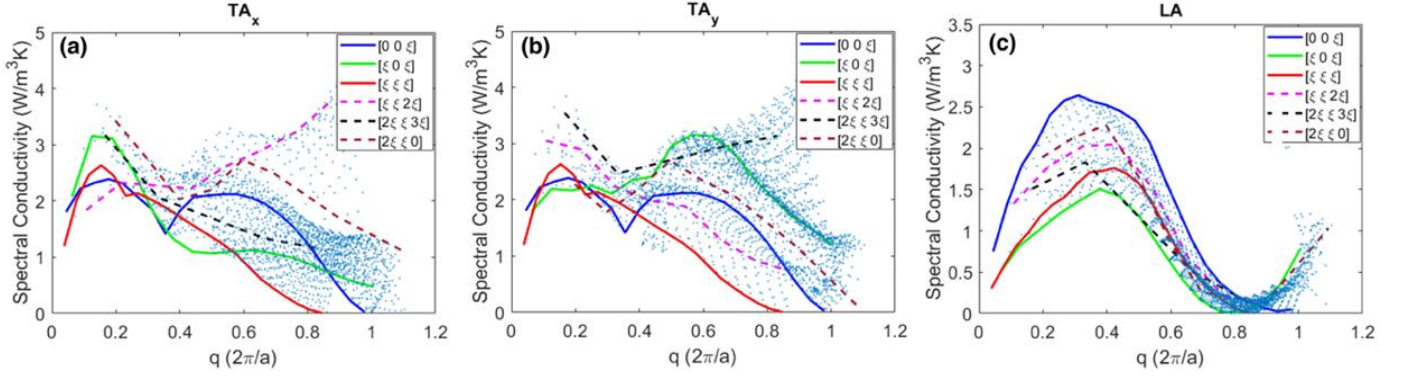


FIG. 6. Spectral conductivity profiles for acoustic modes (a) TA_x , (b) TA_y and (c) LA using CRG potential.

significantly more to conductivity than high symmetry phonons for ThO_2 . The spread of conductivity values for a fixed q -value can be used as a qualitative indication of the degree of anisotropy. While anisotropic features are most notable in the optical modes, their low contribution to thermal conductivity makes a weak impact on the total conductivity.

Acoustic modes have similar anisotropic features as shown in Fig. 5. Anisotropic features in the spectral conductivity profiles are more evident for $\frac{qa}{2\pi} > \frac{1}{2}$. The spectral conductivity profiles for TA_y mode (Fig. 5b) is highly anisotropic and suggest significant contribution from the phonons along low symmetry direction. The spectral conductivity profile for TA_x mode (Fig. 5a) also indicates a contribution from some of the phonons along low symmetry direction. Similar to the case of TO_x mode, these phonons i.e., one along $[\xi, \xi, 2\xi]$ direction, are not bounded by the high symmetry axes. In contrast, these anisotropic features are less obvious in the LA mode (Fig. 5c). In fact, one can classify the LA mode as isotropic. There is also a dip present in the spectral conductivity profile along $[00\xi]$ direction for all acoustic modes, located at 0.2 for LA and 0.45 for TA modes.

The spectral conductivity anisotropy is stronger in the model system represented by EIP-CRG, an empirical interatomic potential, exhibits a stronger anisotropy. Figure 6 depicts the spectral thermal conductivity profile for the acoustic modes calculated using the CRG potential. Similar to the case of DFT-LDA calculation, the TA modes have large thermal conductivity contributions from phonons along low symmetry directions (Fig. 6 a and b).

However, with EIP-CRG, the anisotropic features in the LA mode are more pronounced over q -values ranging from $0.2 < \frac{qa}{2\pi} < 0.4$. Therefore EIP-CRG derived phonon can serve as a model for higher anisotropy systems. It is to be noted that the contribution of optical branches to thermal conductivity is much more significant with EIP-

CRG compared to DFT-LDA as observed from Fig. 3. The spectral conductivity profiles for acoustic modes along $[00\xi]$ direction have a dip similar to the DFT-LDA case.

D. Iso-surface plots

An alternative method to represent the anisotropic feature is to consider the contribution of all modes propagating in all-direction using a contour plot similar to the q -iso-surface plot shown in Fig. 1. For this, we chose irreducible representation using a 2D surface plot, where we only plot the wavevectors contained within the IBZ shown in Fig. 2(b) corresponding to a spherical shell with a radius $\frac{qa}{2\pi} = 0.62$. From Fig. 7, it can be observed that low symmetry directions optical modes represented by the central portions of the polar plots have significantly greater contributions compared to the high symmetry phonons located at the corners. This is especially notable in the case of $1TO_x$ mode (Fig. 7d), which has maxima along $[hkl]=[210]$. The $1TO_y$ mode (Fig. 7e) also shows a significant contribution from the off-axial regions. On the other hand, for the $1LO$ (Fig. 7f), the anisotropy effect is weak, and LA mode appears isotropic consistent with Fig. 3(c). In TA modes, for the most part, the contribution of low-symmetry acoustic modes is bounded by the high symmetry phonons. Similar polar plots for EIP-CRG calculation are available in supplementary documents and unlike the DFT-LDA case, it reveals strong anisotropy within LA mode.

E. Analysis by phonon group velocity and lifetime

Here, we discuss the source of the anisotropic thermal conductivity contributions of different modes in ThO_2 . The spectral conductivity profiles and polar plots are presented in Figs. 4-7 illustrate the significant contribution of low-symmetry phonons to thermal conductivity. Here, we take a closer look at the phonon velocity and lifetimes as both contribute to the calculation of thermal conductivity (Eq. 1). Figure 8 shows the phonon velocities and lifetimes for

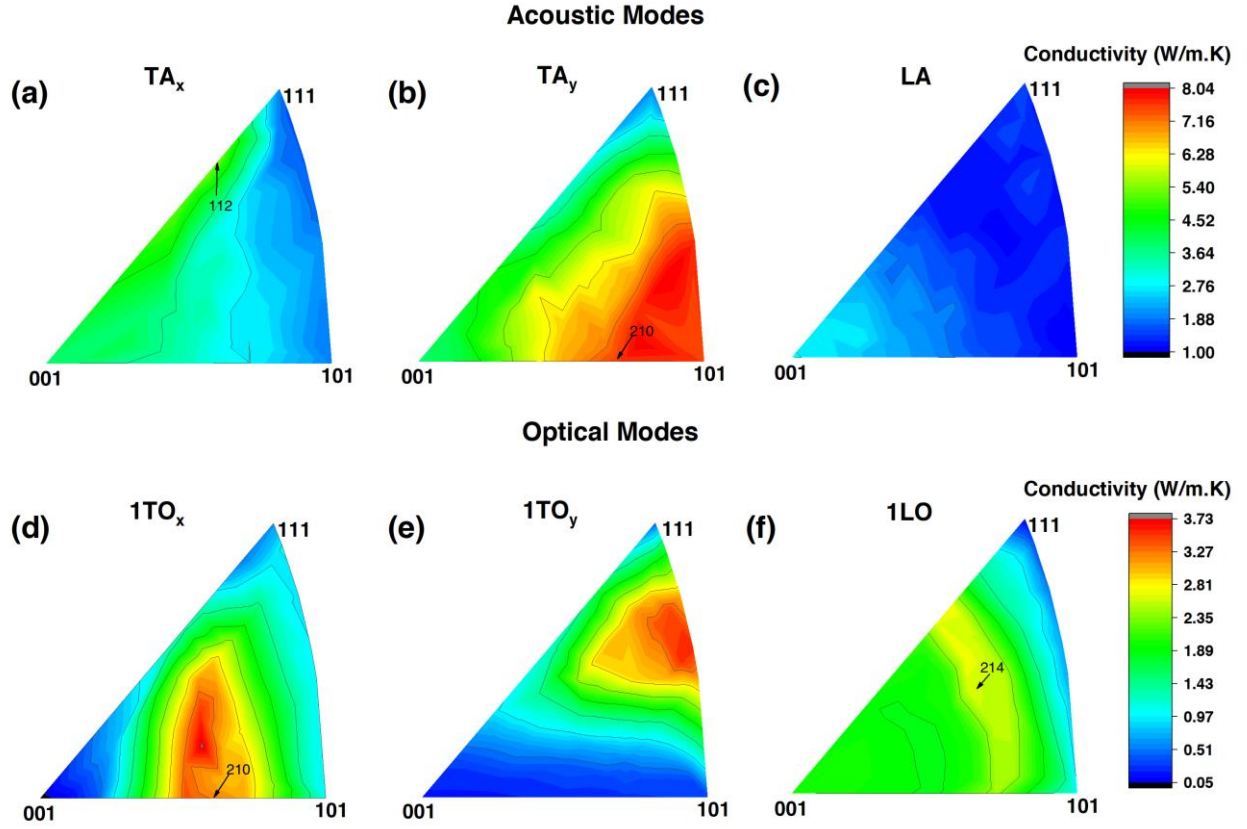


FIG. 7. Inverse polar plots of the acoustic modes (a) TA_x , (b) TA_y , (c) LA , and optical modes (d) $1TO_x$, (e) $1TO_y$, (f) $1LO$ using DFT-LDA at $q=0.620$. Arrows indicate particular modes discussed in the text.

selected acoustic and optical modes obtained from DFT-LDA IFC (plots for all 9 modes are available in the supplementary document). It should be emphasized that comparison should be done on modes that have the same q -vector magnitude. In the case of the TA_x , some modes are seen to have higher velocity but lower lifetimes than the high-symmetry modes. In particular, $[\xi, \xi, 2\xi]$ mode appears to have the largest velocity, the same direction has the largest contribution to the spectral conductivity profiles (Fig. 5). In the case of TA_y and LA modes, we observed that the phonon velocities and lifetime profiles for off-axis phonons are bounded by the high-symmetry ones. One interesting observation is that the conductivity contribution of $[00\xi]$ and $[\xi\xi\xi]$ phonons vanish at the zone boundary. However, the contribution of low symmetry phonons and along $[\xi 0\xi]$ and $[2\xi, \xi, 0]$ are large at zone boundaries. All these zone boundary effects correlate with the magnitude of the velocity (Fig. 8). This results in high spectral conductivity for some of the low-symmetry phonons at high values of q in Fig. 5.

In the case of the optical modes, we have seen a high level of anisotropy in the $1TO_x$ mode (Fig. 4a). Examination of plots in Fig. 8(c) reveals that the velocity for off-axis phonon is significantly larger than for high-

symmetry ones. Another notable observation, unlike acoustic modes, the distribution of TO_x mode's lifetime is not bounded by high-symmetry phonons. The combined effect of velocity and lifetime results in large anisotropy in spectral conductivity profiles. Comparing between phonons along $[\xi\xi\xi]$ and $[2\xi, \xi, 0]$ direction, one can observe that they have comparable lifetimes. However, the ones along $[2\xi, \xi, 0]$ are significantly faster, resulting in a very high spectral conductivity. Thus, combining the results for both acoustic and optical modes (Fig. 8), a larger phonon velocity along low-symmetry directions can be attributed as the primary factor leading to the observed anisotropic behavior in spectral conductivity.

As already pointed out, the spectral conductivity plots show a consistent dip in the spectral profiles of the acoustic modes, especially along $[00\xi]$ direction appearing in $\frac{qa}{2\pi} = 0.38 - 0.52$ range for both TA modes, which corresponds to a frequency range of 2~2.5 THz. We speculate that this dip is related to both the magnitude of the three-phonon scattering phase space and scattering strength. The former is quantified by the joint density of states (JDOS) D_2 [37]. We noticed a sharp rise in the scattering strength of the phonons for the TA mode located close to the q -values of the dip (see Fig. S5). The value of D_2 also increases in the

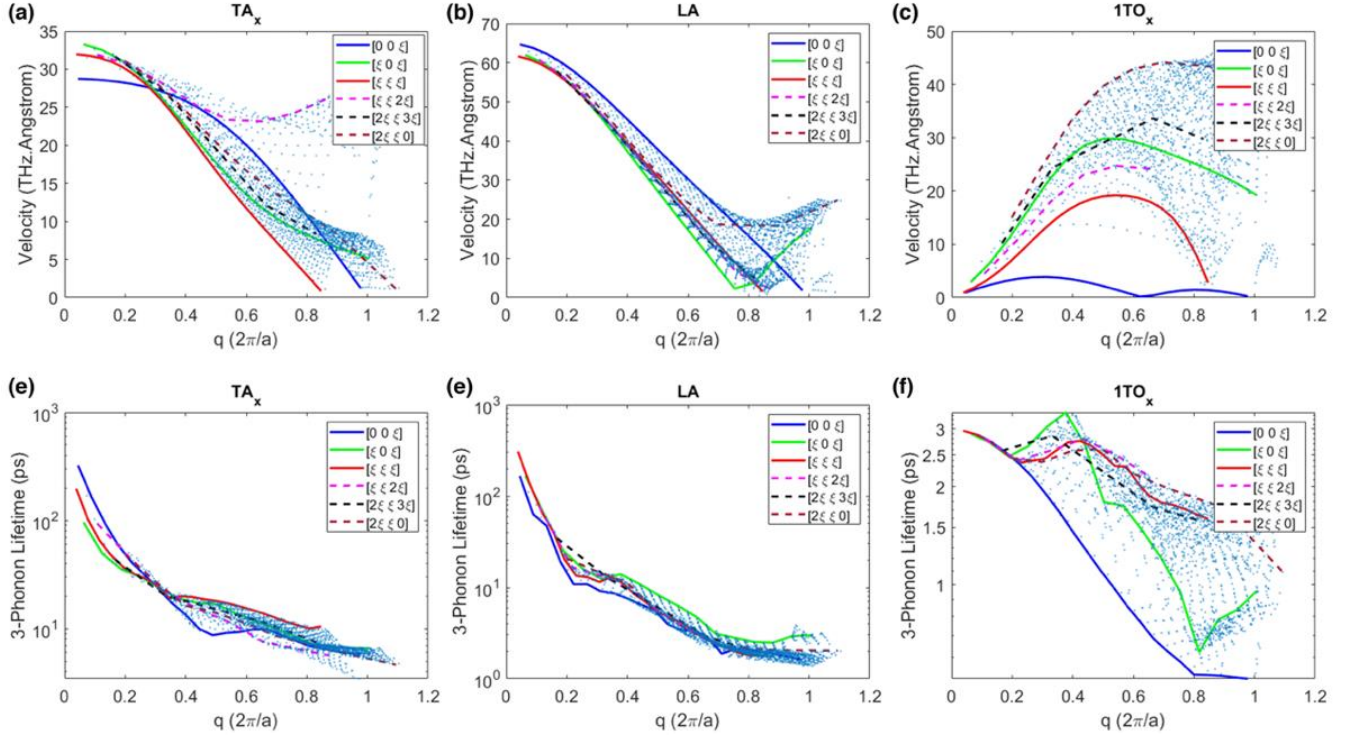


FIG. 8. Phonon group velocities (top) and lifetimes (bottom) for TA_x , LA , and $1TO_x$ mode from DFT-LDA.

range corresponding to the dip's frequency and q point. Both the scattering strength and phase space lower the thermal conductivity by enhancing the 3-phonon scattering rate [32,52].

IV. ISOTROPIC BULK CONDUCTIVITY

It should be emphasized that despite the anisotropic contribution of different modes, the total bulk conductivity is isotropic as expected for materials with cubic symmetry. This is because thermal conductivity is a second-rank tensor and any physical property having a second-rank tensor will always be isotropic for a cubic material [53]. This stems from Neumann's principle [35] which states that the symmetry elements of physical property, in this case, thermal conductivity, must include all the symmetry elements of the point group of the crystal. In other words, the thermal conductivity tensor in ThO_2 cannot possess a lower symmetry than the cubic octahedral (O_h) symmetry group it belongs to. In the appendix, we provide proof that conductivity calculation using Eq. 1 indeed results in isotropic conductivity and demonstrate that this isotropy is dictated by the symmetry of the $\mathbf{v} \otimes \mathbf{v}$ product. Mathematically, this leads to a diagonal conductivity tensor having a single independent component which indicates isotropic thermal conductivity.

It is also important to emphasize that phonon linewidth anisotropy is not an indication of conductivity anisotropy. Anisotropic features for phonon linewidth have been experimentally found for UO_2 and reported by Paolasini et. al [14]. However, the authors incorrectly inferred that this anisotropic behavior leads to anisotropic bulk thermal conductivity.

V. BOUNDARY SCATTERING INDUCED ANISOTROPY

So far, our discussion has focused on the anisotropic nature of the phonons, and based on the discussion in the last section, we concluded that the bulk conductivity in ThO_2 and fluorite is isotropic. However, there are special cases where the phonon anisotropy can lead to an induced conductivity anisotropy. It is expected to occur when some external perturbation leads to a reduction in the symmetry of the phonon lifetime. One example involves the thermal conductivity calculation using NEMD. Figure 9 shows a computationally measured thermal conductivity of ThO_2 as a function of simulation cells length and crystallographic orientation of the cells with respect to heat flux. We observe, not only that the thermal conductivity depends on the cell size but also on crystal orientation. Notably, anisotropy is negligible for large cells where all size effects vanish as expected. This size dependence has

been attributed to ballistic effects, where the phonons with mean free path (MFP) larger than the cell size do not contribute to thermal conductivity [54]. We observe that while for [110] and [111] orientations, the conductivity reduction is smaller compared to [100].

We analyze this behavior using BTE with the inclusion of a boundary scattering term. For comparative analysis with the NEMD results, we included a boundary scattering term in our BTE calculation. The total scattering time, τ was expressed using Matthiessen's rule as [32,55,56]:

$$\frac{1}{\tau} = \frac{1}{\tau_{3ph}} + \frac{2\vec{v} \cdot \hat{h}}{L} \quad (4)$$

Here τ_{3ph} is the three-photon scattering time obtained from Phono3py and 2nd term is the boundary scattering time. The boundary scattering time is expressed in terms of the simulation cell length (L) and the inner product of the phonon velocity (\vec{v}) and the directional vector (\hat{h}). This direction specifies crystalline orientation with respect to the boundaries defined by the finite length of the NEMD cell. BTE conductivity values in the limit of large cells are larger. Several factors can contribute to this. First, BTE is not capturing phonon interactions resulting from beyond 3rd-order anharmonicity, while NEMD does [57]. Additionally, phonon distribution in NEMD lacks quantum effects present in BTE. We noticed that the NEMD results showed a significant level of anisotropy compared to the BTE, this could also be related to the same factors that lead to a discrepancy in bulk values. Next, regarding the actual origin of the anisotropic conductivity, we attribute this to the length of the simulation cell being comparable to the mean free path (MFP) of the phonons. We see that the simple boundary scattering expression used in BTE is unable to capture the apparent anisotropy as NEMD does. Nevertheless, the trends are similar which suggests that size effects impact [001]-oriented cells more than [101] and [111]-oriented ones. A simple explanation for this can be obtained by examining spectral conductivity plots, particularly focusing on low q -value phonons that have the largest MFP and are most impacted by size effects. For the acoustic modes at low q -values, the contribution of the [001]-phonons is larger than [101] or [111] ones (Fig.5). In small cell sizes, this impacts [001]-phonons the most, as a result leading to the larger reduction in conductivity for cells oriented along this direction. Similar observations can be made from the 3D velocity plots in Fig. 1 for the low value of $\frac{qa}{2\pi} = 0.1$. For both the transverse acoustic modes, phonons have low velocity in the [001] direction compared to the [101] and [111] directions. That means the phonons will scatter heavily in [101] and [111] directions, whereas a weak scattering is observed in the [001], resulting in a

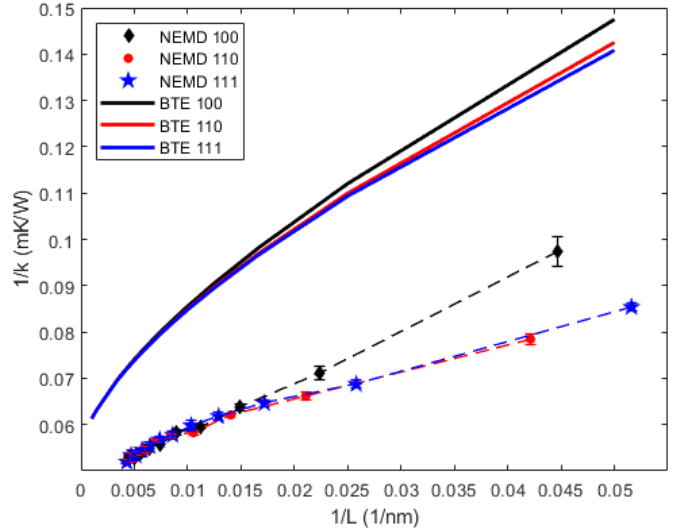


FIG. 9. Thermal conductivity as a function of crystal orientation and simulation cell length using NEMD and BTE.

relatively high contribution for [001]-phonons [58]. The scope of this anisotropic behavior is limited to the contribution of off-axial phonons towards conductivity calculated inside a finite simulation cell. If the size effect of the simulation cell can be eliminated, in other words, if infinite cell length is assumed as for bulk material, the thermal conductivity remains the same along all directions. These observations emphasize the importance of size-dependent analysis when using NEMD. These same arguments provide an explanation for the recent reports of anisotropic conductivity in fluorite oxides based on the result of NEMD calculations [6,12,14].

VI. DEFECT SCATTERING

Next, we analyze the implications of the anisotropic phonon structure on phonon scattering with defects. Consideration of point defects, such as vacancies and interstitials is important for understanding the impact of damage introduced by energetic particles in nuclear fuels [7,25,30,31,61]. The defect scattering rate of phonons depends on the density of state (DOS) of available modes that a phonon can scatter into [2]. These available states are characterized by the same frequency and comparable eigenvectors [59]. First-principles BTE calculation that accounts for phonon-isotope scattering effect along with intrinsic phonon-phonon interaction, has been implemented within the phono3py package [60]. Therefore, to consider the impact of Th and O vacancies, we treat them as mass defects located on Th and O sites. This simplified treatment allows us to leverage the existing isotopic scattering module within Phono3py.

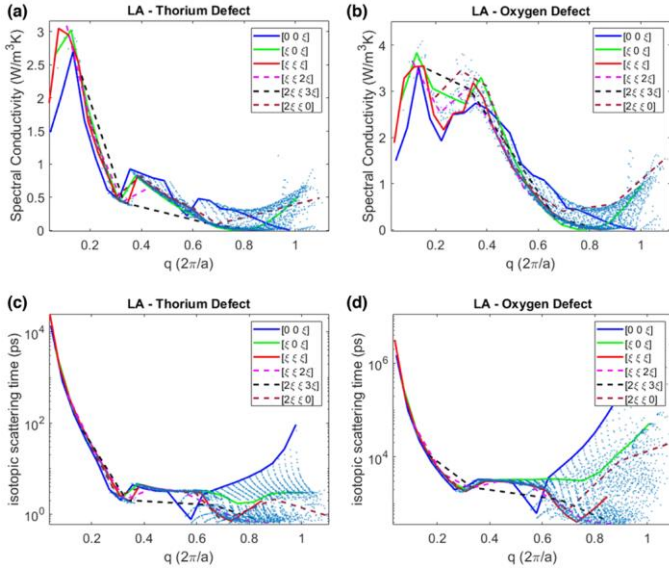


FIG. 10. (a-b) Spectral conductivity profiles accounting for both the three-phonon scattering and isotopic scattering (c-d) isotopic scattering lifetimes in ThO_2 with thorium and oxygen mass defect.

Figure 10 presents the result for both types of defects in the case of the LA mode (the rest of the acoustic and optical mode results can be found in the supplementary material). We can observe that the isotopic scattering time for the acoustic modes is shorter by a couple of orders of magnitude than the optical ones in the case of Th defect sites and the opposite in the case of oxygen defects. This is because in acoustic (optical) mode the phonon-isotope interaction is largely influenced by the heavier (lighter) atom of the unit cell due to its enhanced atomic motion [62–64]. So, the isotopic scattering rate is increased significantly in the acoustic (optical) mode for Th (O) defect sites. This leads to diminished anisotropic features when strong phonon-isotope scattering is present (acoustic modes for Th defects).

We also noticed a steep increase in the isotopic scattering time along $[00\xi]$ direction for $\frac{qa}{2\pi} > 0.6$ in the LA modes. In the past, it has been reported that the isotopic scattering rate rapidly increases near the zone boundary or at high-frequency values, with a dependency larger than the fourth-order of frequency [59,65]. This is due to an increase in the phonon density of states of the decaying phonons at a higher frequency. Phonons in LA mode are predicted theoretically [66], and later experimentally validated [67], to have much stronger scattering than in the TA modes with a dependence on the fifth order of frequency. This is in accordance with our findings with the exception being the $[00\xi]$ direction. Interestingly, the spectral conductivity remained a downward profile even with much weaker isotopic scattering along that direction

(Fig.10 a&b). This might be due to very low phonon velocity and short 3-phonon scattering time which eventually lowers the conductivity. Nevertheless, the role the defects play in dictating the nature of anisotropy through isotopic scattering can be utilized in technological applications.

Another important aspect of anisotropic features observed in the acoustic branches can be its potential connection to non-destructive surface imaging. Elastic anisotropy has been previously utilized to image grain boundaries and measure the orientation of the crystal surface [11,68,69]. Since most of the single crystals are elastically anisotropic, their orientation-dependent velocity profile has been used to gain information on the grain orientation. A similar method can be implemented in the case of thermal anisotropy to capture the microstructural information of the material. However, unlike elastic anisotropy which can be represented by a single scalar term Zener ratio [70], thermal anisotropy has much more complexity as it is sensitive to several other parameters like phonon frequency and q-point vector. This leaves scope for future investigation of this method to incorporate thermal anisotropy.

VII. CONCLUSIONS

In conclusion, we have calculated the lattice thermal conductivity of ThO_2 based on first-principles calculation (DFT) using two contrasting approaches. One of them focuses on only the phonons along high-symmetry axes while the other considers all the phonons to calculate conductivity. The spectral conductivity profiles and iso-surface plots showed strong signs of phonon anisotropy, particularly in the TA_y and the optical modes. Although this phonon anisotropy does not affect the bulk anisotropy in ThO_2 , the size-dependent NEMD results presented a case where anisotropic thermal conductivity is observed. The inclusion of boundary scattering terms in BTE calculation also resulted in similar trends which demonstrated how phonon anisotropy leads to anisotropic conductivity when the cubic symmetry of phonon lifetimes is lifted. Finally, analysis of the potential impact of a defective structure under the framework of isotopic scattering showed a strong correlation between anisotropy, vibrational mode, and vacancy atom. The comprehensive analysis of the phonon anisotropy in ThO_2 presented here, can provide better insight for accurately treating the intricacy involved in characterizing the thermal transport. Focusing on the high energy carrying phonons one can develop materials with a tailored thermal conductivity that can be utilized in nano and micro-scale energy applications.

ACKNOWLEDGEMENTS

This work was supported by Center for Thermal Energy Transport under Irradiation (TETI), an Energy Frontier Research Center funded by the U.S. Department of Energy, Office of Science, and Office of Basic Energy Sciences.

APPENDIX: PROOF OF ANISOTROPIC CONDUCTIVITY IN FLUORITE OXIDES

Fluorite has an $Fm\bar{3}m$ structure with O_h symmetry of face-centered cubic crystal whose Brillouin zone is represented by a truncated octahedron. Phonon properties can be evaluated within the irreducible Brillouin zone (IBZ) defined by the shaded wedge in Fig. 2. To evaluate the full BZ one applies 48 transformations R_i needed to populate the full BZ. When only intrinsic 3-phonon scattering exists, the system retains the O_h symmetry.

If one is interested in conductivity along a particular direction \hat{n} , it is evaluated as a summation over each point in the BZ:

$$\kappa_{\hat{n}} = \frac{1}{V_0} \sum_{q \in BZ} C_q \tau_q |\hat{n} \cdot \vec{v}|^2, \quad (A1)$$

where τ_q and C_q are the group velocity and heat capacity for a point in the q -space inside BZ. This can be rewritten by summation over the IBZ subject to a condition that τ_q retains the O_h symmetry one can write,

$$\kappa_{\hat{n}} = \frac{1}{V_0} \sum_{q \in IBZ} C_q \tau_q \sum_{r=\{1:48\}} |n_{\alpha} R_{r,\alpha\beta} v_{\beta}|^2 \quad (A2)$$

The inner sum in Eq. A2 can be evaluated analytically to show that:

$$\begin{aligned} \sum_{r=\{1:48\}} |n_{\alpha} R_{r,\alpha\beta} v_{\beta}|^2 &= \sum_{r=\{1:48\}} |R_{r,\alpha\beta}^T n_{\beta} v_{\alpha}|^2 \\ &= 16(v_x^2 + v_y^2 + v_z^2) \end{aligned} \quad (A3)$$

This depends only on the magnitude of the group velocity and is independent of the direction along which conductivity is calculated. This indicates that even though phonons have strong anisotropy their impact on thermal conductivity is isotropic and is attributed to the symmetry of the FCC structure.

Alternatively, one can calculate the conductivity tensor and show that a diagonal matrix with only a single

independent component remains, consistent with Neumann's principle.

$$\begin{aligned} \sum_{r=\{1:48\}} R_{\alpha\gamma} v_{\gamma} R_{\beta\delta} v_{\delta} \\ = 16(v_x^2 + v_y^2 + v_z^2) \begin{bmatrix} 1 & 0 & 0 \\ 0 & 1 & 0 \\ 0 & 0 & 1 \end{bmatrix} \end{aligned} \quad (A4)$$

When symmetry breaking phonon scattering processes are present, such as in the case of scattering from the boundaries, the simplification present in Eq. A2 is no longer applicable. If one accounts for the boundary scattering assuming that all of the boundaries are oriented with a surface normal \hat{b} , the scattering rate can be expressed as,

$$\frac{1}{\tau_B} = \frac{2|\vec{v} \cdot \hat{b}|}{L} \quad (A5)$$

This lift the symmetry for scattering rate and the inner summation in the previous expression (Eq. A2) can no longer be performed with τ_q as a common factor. However, τ_q is expected to have the symmetry of \hat{b} directions, such as (100), (110), and (111) will have C_{4v} , C_{2v} , and C_{3v} symmetries respectively.

References:

- [1] J. W. L. Pang, W. J. L. Buyers, A. Chernatynskiy, M. D. Lumsden, B. C. Larson, and S. R. Phillpot, *Phonon Lifetime Investigation of Anharmonicity and Thermal Conductivity of UO₂ by Neutron Scattering and Theory*, Phys. Rev. Lett. **110**, 157401 (2013).
- [2] D. H. Hurley, A. El-Azab, M. S. Bryan, M. W. D. Cooper, C. A. Dennett, K. Gofryk, L. He, M. Khafizov, G. H. Lander, M. E. Manley, J. M. Mann, C. A. Marianetti, K. Rickert, F. A. Selim, M. R. Tonks, and J. P. Wharry, *Thermal Energy Transport in Oxide Nuclear Fuel*, Chem. Rev. **122**, 3711 (2022).
- [3] Q. Yin and S. Y. Savrasov, *Origin of Low Thermal Conductivity in Nuclear Fuels*, Phys. Rev. Lett. **100**, 225504 (2008).
- [4] L. Fu, M. Kornbluth, Z. Cheng, and C. A. Marianetti, *Group Theoretical Approach to Computing Phonons and Their Interactions*, Phys. Rev. B **100**, 014303 (2019).
- [5] M. Jin, M. Khafizov, C. Jiang, S. Zhou, C. A. Marianetti, M. S. Bryan, M. E. Manley, and D. H. Hurley, *Assessment of Empirical Interatomic Potential to Predict Thermal Conductivity in ThO₂ and UO₂*, J. Phys.: Condens. Matter **33**, 275402 (2021).
- [6] L. Malakkal, A. Prasad, D. Oladimeji, E. Jossou, J. Ranasinghe, B. Szpunar, L. Bichler, and J. Szpunar, *Atomistic and Experimental Study on Thermal Conductivity of Bulk and Porous Cerium Dioxide*, Sci Rep **9**, 6326 (2019).

- [7] C. A. Dennett, Z. Hua, A. Khanolkar, T. Yao, P. K. Morgan, T. A. Prusnick, N. Poudel, A. French, K. Gofryk, L. He, L. Shao, M. Khafizov, D. B. Turner, J. M. Mann, and D. H. Hurley, *The Influence of Lattice Defects, Recombination, and Clustering on Thermal Transport in Single Crystal Thorium Dioxide*, *APL Materials* **8**, 111103 (2020).
- [8] K. Rickert, T. A. Prusnick, E. Hunt, A. French, D. B. Turner, C. A. Dennett, L. Shao, and J. M. Mann, *Raman and Photoluminescence Evaluation of Ion-Induced Damage Uniformity in ThO₂*, *Nuclear Instruments and Methods in Physics Research Section B: Beam Interactions with Materials and Atoms* **515**, 69 (2022).
- [9] T. Taniguchi, T. Watanabe, N. Sugiyama, A. K. Subramani, H. Wagata, N. Matsushita, and M. Yoshimura, *Identifying Defects in Ceria-Based Nanocrystals by UV Resonance Raman Spectroscopy*, *J. Phys. Chem. C* **113**, 19789 (2009).
- [10] Y. Wang, D. H. Hurley, Z. Hua, T. Pezeril, S. Raetz, V. E. Gusev, V. Tournat, and M. Khafizov, *Imaging Grain Microstructure in a Model Ceramic Energy Material with Optically Generated Coherent Acoustic Phonons*, *Nat Commun* **11**, 1 (2020).
- [11] Y. Wang, D. H. Hurley, Z. Hua, G. Sha, S. Raetz, V. E. Gusev, and M. Khafizov, *Nondestructive Characterization of Polycrystalline 3D Microstructure with Time-Domain Brillouin Scattering*, *Scripta Materialia* **166**, 34 (2019).
- [12] K. Gofryk, S. Du, C. R. Stanek, J. C. Lashley, X.-Y. Liu, R. K. Schulze, J. L. Smith, D. J. Safarik, D. D. Byler, K. J. McClellan, B. P. Uberuaga, B. L. Scott, and D. A. Andersson, *Anisotropic Thermal Conductivity in Uranium Dioxide*, *Nat Commun* **5**, 4551 (2014).
- [13] M. J. Rahman, B. Szpunar, and J. A. Szpunar, *The Induced Anisotropy in Thermal Conductivity of Thorium Dioxide and Cerium Dioxide*, *Mater. Res. Express* **4**, 075512 (2017).
- [14] L. Paolasini, D. Chaney, A. Bosak, G. H. Lander, and R. Caciuffo, *Anisotropy in Cubic UO₂ Caused by Electron-Lattice Interactions*, *Phys. Rev. B* **104**, 024305 (2021).
- [15] W. B. Lacina and P. S. Pershan, *Phonon Optical Properties of Ca_{1-x}Sr_xF₂*, *Phys. Rev. B* **1**, 1765 (1970).
- [16] K. Clausen, W. Hayes, J. E. Macdonald, R. Osborn, P. G. Schnabel, M. T. Hutchings, and A. Magerl, *Inelastic Neutron Scattering Investigation of the Lattice Dynamics of ThO₂ and CeO₂*, *J. Chem. Soc., Faraday Trans. 2* **83**, 1109 (1987).
- [17] M. S. Bryan, L. Fu, K. Rickert, D. Turner, T. A. Prusnick, J. M. Mann, D. L. Abernathy, C. A. Marianetti, and M. E. Manley, *Nonlinear Propagating Modes beyond the Phonons in Fluorite-Structured Crystals*, *Commun Phys* **3**, 1 (2020).
- [18] D. L. Abernathy, M. B. Stone, M. J. Loguillo, M. S. Lucas, O. Delaire, X. Tang, J. Y. Y. Lin, and B. Fultz, *Design and Operation of the Wide Angular-Range Chopper Spectrometer ARCS at the Spallation Neutron Source*, *Review of Scientific Instruments* **83**, 015114 (2012).
- [19] E. Xiao, H. Ma, M. S. Bryan, L. Fu, J. M. Mann, B. Winn, D. L. Abernathy, R. P. Hermann, A. R. Khanolkar, C. A. Dennett, D. H. Hurley, M. E. Manley, and C. A. Marianetti, *Validating First-Principles Phonon Lifetimes via Inelastic Neutron Scattering*, *ArXiv:2202.11041 [Cond-Mat]* (2022).
- [20] M. Liu, D. Dong, R. Peng, J. Gao, J. Diwu, X. Liu, and G. Meng, *YSZ-Based SOFC with Modified Electrode/Electrolyte Interfaces for Operating at Temperature Lower than 650°C*, *Journal of Power Sources* **180**, 215 (2008).
- [21] K. Zheng, B. C. H. Steele, M. Sahibzada, and I. S. Metcalfe, *Solid Oxide Fuel Cells Based on Ce(Gd)O_{2-x} Electrolytes*, *Solid State Ionics* **86-88**, 1241 (1996).
- [22] A. Trovarelli, C. de Leitenburg, M. Boaro, and G. Dolcetti, *The Utilization of Ceria in Industrial Catalysis*, *Catalysis Today* **50**, 353 (1999).
- [23] D. A. Andersson, S. I. Simak, B. Johansson, I. A. Abrikosov, and N. V. Skorodumova, *Modeling of CeO₂, Ce₂O₃ and CeO_{2-x} in the LDA+U Formalism*, *Phys. Rev. B* **75**, 035109 (2007).
- [24] S. L. Dudarev, D. N. Manh, and A. P. Sutton, *Effect of Mott-Hubbard Correlations on the Electronic Structure and Structural Stability of Uranium Dioxide*, *Philosophical Magazine B* **75**, 613 (1997).
- [25] L. Malakkal, A. Prasad, E. Jossou, J. Ranasinghe, B. Szpunar, L. Bichler, and J. Szpunar, *Thermal Conductivity of Bulk and Porous ThO₂: Atomistic and Experimental Study*, *Journal of Alloys and Compounds* **798**, 507 (2019).
- [26] P. S. Ghosh, A. Arya, G. K. Dey, N. Kuganathan, and R. W. Grimes, *A Computational Study on the Superionic Behaviour of ThO₂*, *Phys. Chem. Chem. Phys.* **18**, 31494 (2016).
- [27] L. Lindsay, D. A. Broido, and T. L. Reinecke, *Ab Initio Thermal Transport in Compound Semiconductors*, *Phys. Rev. B* **87**, 165201 (2013).
- [28] M. W. D. Cooper, S. C. Middleburgh, and R. W. Grimes, *Modelling the Thermal Conductivity of (U_xTh_{1-x})O₂ and (U_xPu_{1-x})O₂*, *Journal of Nuclear Materials* **466**, 29 (2015).
- [29] T. Arima, K. Yoshida, T. Matsumoto, Y. Inagaki, and K. Idemitsu, *Thermal Conductivities of ThO₂, NpO₂ and Their Related Oxides: Molecular Dynamics Study*, *Journal of Nuclear Materials* **445**, 175 (2014).
- [30] Y. Lu, Y. Yang, and P. Zhang, *Thermodynamic Properties and Structural Stability of Thorium Dioxide*, *J. Phys.: Condens. Matter* **24**, 225801 (2012).
- [31] J. Liu, Z. Dai, X. Yang, Y. Zhao, and S. Meng, *Lattice Thermodynamic Behavior in Nuclear Fuel ThO₂ from First Principles*, *Journal of Nuclear Materials* **511**, 11 (2018).
- [32] J. M. Ziman, *Electrons and Phonons: The Theory of Transport Phenomena in Solids* (Oxford University Press, Oxford, 2001).
- [33] W. R. Deskins, A. Hamed, T. Kumagai, C. A. Dennett, J. Peng, M. Khafizov, D. Hurley, and A. El-Azab, *Thermal Conductivity of ThO₂: Effect of Point Defect Disorder*, *Journal of Applied Physics* **129**, 075102 (2021).

- [34] J. Park, E. B. Farfán, K. Mitchell, A. Resnick, C. Enriquez, and T. Yee, *Sensitivity of Thermal Transport in Thorium Dioxide to Defects*, *Journal of Nuclear Materials* **504**, 198 (2018).
- [35] R. E. Newnham, *Properties of Materials: Anisotropy, Symmetry, Structure* (OUP Oxford, 2005).
- [36] L. Chaput, *Direct Solution to the Linearized Phonon Boltzmann Equation*, *Phys. Rev. Lett.* **110**, 265506 (2013).
- [37] A. Togo, L. Chaput, and I. Tanaka, *Distributions of Phonon Lifetimes in Brillouin Zones*, *Phys. Rev. B* **91**, 094306 (2015).
- [38] P. G. Klemens, *Thermal Conductivity and Lattice Vibrational Modes*, in *Solid State Physics*, edited by F. Seitz and D. Turnbull, Vol. 7 (Academic Press, 1958), pp. 1–98.
- [39] A. Togo and I. Tanaka, *First Principles Phonon Calculations in Materials Science*, *Scripta Materialia* **108**, 1 (2015).
- [40] S. Plimpton, *Fast Parallel Algorithms for Short-Range Molecular Dynamics*, *Journal of Computational Physics* **117**, 1 (1995).
- [41] M. W. D. Cooper, M. J. D. Rushton, and R. W. Grimes, *A Many-Body Potential Approach to Modelling the Thermomechanical Properties of Actinide Oxides*, *J. Phys.: Condens. Matter* **26**, 105401 (2014).
- [42] G. Kresse and J. Furthmüller, *Efficiency of Ab-Initio Total Energy Calculations for Metals and Semiconductors Using a Plane-Wave Basis Set*, *Computational Materials Science* **6**, 15 (1996).
- [43] J.-L. Calais, *Density-Functional Theory of Atoms and Molecules*. R.G. Parr and W. Yang, *Oxford University Press, New York, Oxford, 1989. IX + 333 Pp. Price £45.00*, *International Journal of Quantum Chemistry* **47**, 101 (1993).
- [44] M. A. Mathis, A. Khanolkar, L. Fu, M. S. Bryan, C. A. Dennett, K. Rickert, J. M. Mann, B. Winn, D. L. Abernathy, M. E. Manley, D. H. Hurley, and C. A. Marianetti, *The Generalized Quasiharmonic Approximation via Space Group Irreducible Derivatives*, *ArXiv:2202.14016 [Cond-Mat]* (2022).
- [45] L. F. Huang, P. L. Gong, and Z. Zeng, *Correlation between Structure, Phonon Spectra, Thermal Expansion, and Thermomechanics of Single-Layer MoS₂*, *Phys. Rev. B* **90**, 045409 (2014).
- [46] *Introduction to Solid State Physics, 8th Edition / Wiley*, <https://www.wiley.com/en-us/Introduction+to+Solid+State+Physics%2C+8th+Edition-p-9780471415268>.
- [47] A. Valentin, J. Sée, S. Galdin-Retailleau, and P. Dollfus, *Study of Phonon Modes in Silicon Nanocrystals Using the Adiabatic Bond Charge Model*, *J. Phys.: Condens. Matter* **20**, 145213 (2008).
- [48] X. Wang and B. Huang, *Computational Study of In-Plane Phonon Transport in Si Thin Films*, *Sci Rep* **4**, 6399 (2014).
- [49] R. L. Xu, M. Muñoz Rojo, S. M. Islam, A. Sood, B. Vareskic, A. Katre, N. Mingo, K. E. Goodson, H. G. Xing, D. Jena, and E. Pop, *Thermal Conductivity of Crystalline AlN and the Influence of Atomic-Scale Defects*, *Journal of Applied Physics* **126**, 185105 (2019).
- [50] P. Pavone, K. Karch, O. Schütt, D. Strauch, W. Windl, P. Giannozzi, and S. Baroni, *Ab Initio Lattice Dynamics of Diamond*, *Phys. Rev. B* **48**, 3156 (1993).
- [51] J. Serrano, J. Stempfer, M. Cardona, M. Schwoerer-Böhning, H. Requardt, M. Lorenzen, B. Stojetz, P. Pavone, and W. J. Choyke, *Determination of the Phonon Dispersion of Zinc Blende (3C) Silicon Carbide by Inelastic x-Ray Scattering*, *Appl. Phys. Lett.* **80**, 4360 (2002).
- [52] L. Lindsay and D. A. Broido, *Three-Phonon Phase Space and Lattice Thermal Conductivity in Semiconductors*, *J. Phys.: Condens. Matter* **20**, 165209 (2008).
- [53] L. E. Murr, *Examples of Tensor Properties Using Matrix Fundamentals (A Physical Property)*, in *Handbook of Materials Structures, Properties, Processing and Performance*, edited by L. E. Murr (Springer International Publishing, Cham, 2015), pp. 343–357.
- [54] J. Park, E. B. Farfán, and C. Enriquez, *Thermal Transport in Thorium Dioxide*, *Nuclear Engineering and Technology* **50**, 731 (2018).
- [55] P. Steiner, S. Adnan, M. S. Ergoktas, J. Barrier, X. Yu, V. Orts, G. Bakan, J. Aze, Y. Malevich, K. Wang, P. Cataldi, M. Bisset, S. Balci, S. Suzer, M. Khafizov, and C. Kocabas, *Electrically Controlled Heat Transport in Multilayer Graphene*, (2022).
- [56] V. S. Chauhan, J. Pakarinen, T. Yao, L. He, D. H. Hurley, and M. Khafizov, *Indirect Characterization of Point Defects in Proton Irradiated Ceria*, *Materialia* **15**, 101019 (2021).
- [57] T. Tadano, Y. Gohda, and S. Tsuneyuki, *Anharmonic Force Constants Extracted from First-Principles Molecular Dynamics: Applications to Heat Transfer Simulations*, *J. Phys.: Condens. Matter* **26**, 225402 (2014).
- [58] Z. Aksamija and I. Knezevic, *Anisotropy and Boundary Scattering in the Lattice Thermal Conductivity of Silicon Nanomembranes*, *Phys. Rev. B* **82**, 045319 (2010).
- [59] S. Tamura, *Isotope Scattering of Dispersive Phonons in Ge*, *Phys. Rev. B* **27**, 858 (1983).
- [60] L. J. Evitts, S. C. Middleburgh, E. Kardoulaki, I. Ipatova, M. J. D. Rushton, and W. E. Lee, *Influence of Boron Isotope Ratio on the Thermal Conductivity of Uranium Diboride (UB₂) and Zirconium Diboride (ZrB₂)*, *Journal of Nuclear Materials* **528**, 151892 (2020).
- [61] M. Khafizov, M. F. Riyad, Y. Wang, J. Pakarinen, L. He, T. Yao, A. El-Azab, and D. Hurley, *Combining Mesoscale Thermal Transport and X-Ray Diffraction Measurements to Characterize Early-Stage Evolution of Irradiation-Induced Defects in Ceramics*, *Acta Materialia* **193**, 61 (2020).
- [62] L. Lindsay, D. A. Broido, and T. L. Reinecke, *Phonon-Isotope Scattering and Thermal Conductivity in Materials with a Large Isotope Effect: A First-Principles Study*, *Phys. Rev. B* **88**, 144306 (2013).
- [63] L. Lindsay, D. A. Broido, and T. L. Reinecke, *First-Principles Determination of Ultrahigh Thermal Conductivity of Boron Arsenide: A Competitor for Diamond?*, *Phys. Rev. Lett.* **111**, 025901 (2013).

- [64] S. Tamura, *Isotope Scattering of Large-Wave-Vector Phonons in GaAs and InSb: Deformation-Dipole and Overlap-Shell Models*, Phys. Rev. B **30**, 849 (1984).
- [65] W. E. Bron, *Spectroscopy of High-Frequency Phonons*, Rep. Prog. Phys. **43**, 301 (1980).
- [66] R. Orbach and L. A. Vredevoe, *The Attenuation of High Frequency Phonons at Low Temperatures*, Physics Physique Fizika **1**, 91 (1964).
- [67] H. Lengfellner and K. F. Renk, *Anharmonic Decay of Zone-Boundary Phonons Observed by a New Method of Phonon Detection*, Phys. Rev. Lett. **46**, 1210 (1981).
- [68] M. Khafizov, J. Pakarinen, L. He, H. B. Henderson, M. V. Manuel, A. T. Nelson, B. J. Jaques, D. P. Butt, and D. H. Hurley, *Subsurface Imaging of Grain Microstructure Using Picosecond Ultrasonics*, Acta Materialia **112**, 209 (2016).
- [69] D. H. Hurley, O. B. Wright, O. Matsuda, T. Suzuki, S. Tamura, and Y. Sugawara, *Time-Resolved Surface Acoustic Wave Propagation across a Single Grain Boundary*, Phys. Rev. B **73**, 125403 (2006).
- [70] C. M. Zener and S. Siegel, *Elasticity and Anelasticity of Metals.*, J. Phys. Chem. **53**, 1468 (1949).